Article

Interlayer sp^3 Bonds and Chirality at Bilayer Graphene Oxide/Calcium Silicate Hydrate Abnormally Enhance Its Interlayer Stress Transfer

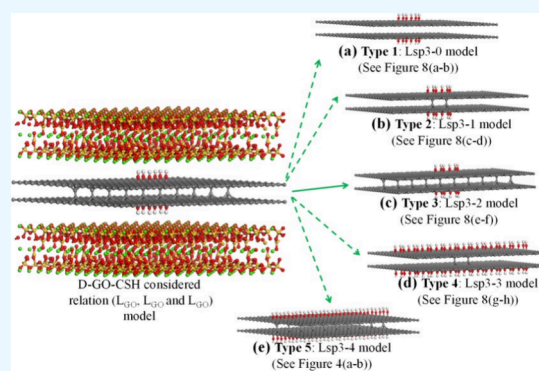Lei Fan,* Fangyuan Song, Jingjing Xu, Hongwei Wang, and Fengzhi Wang

Read Online

ACCESS | Metrics & More | Article Recommendations

ABSTRACT: Graphene oxide (GO) is an ideal reinforcing material with super design capability, which can achieve the combination of strength and toughness. However, the actual effect of GO is far below the theoretical prediction. This is mainly due to the weak interface between the nanofiller and the matrix. In this paper, a controllable method for improving interlayer stress transfer of double-layer graphene oxide/C−S−H (D-GO−CSH)-layered nanostructures is proposed by using interlayer sp^3 bond and chirality. The results show that, compared with the control group, the normalized shear stress and normalized pull-out energy of the OH-sp3 model are increased by 44.93 and 49.25%, respectively, while those of the OO-sp3 model are increased by 32.26 and 31.03%, respectively. The interlayer sp^3 bonds lead to a great enhancement (more than 3 times) in normalized interlayer stress transfer of D-GO−CSH-layered nanostructures while exerting a little opposite effect (about 5%). The improvement effects induced by the interlayer sp^3 bonds are also strongly dependent on their distributions and the chirality of GO. According to the fracture mechanic theory and molecular dynamics results, the strain energy percentage difference (bond length and bond angle) of the zigzag-cen model is 34.8% lower than that of the control group model, which proves that the interlayer sp^3 bonds have a remarkably positive effect on the interlayer stress transfer of D-GO−CSH-layered nanostructures. This provides a new way to further improve the interlayer stress transfer, pull-out energy, and interlayer shear stress of D-GO−CSH-layered nanostructures.

D-GO-CSH considered relation (L$_{GO}$, L$_{GO}$ and L$_{GO}$) model

(a) Type 1: Lsp3-0 model (See Figure 8(a-b))
(b) Type 2: Lsp3-1 model (See Figure 8(c-d))
(c) Type 3: Lsp3-2 model (See Figure 8(e-f))
(d) Type 4: Lsp3-3 model (See Figure 8(g-h))
(e) Type 5: Lsp3-4 model (See Figure 4(a-b))

1. INTRODUCTION

Calcium silicate hydrate (CSH) is one of the main hydration products of concrete materials, accounting for about 60−70% of the total volume.[1] CSH is one of the main sources of concrete strength.[2,3] However, the interlayer of the C−S−H-layered structure is only maintained by van der Waals force and weak ionic bonds. Therefore, using nanomodification technology to optimize the microstructure of C−S−H gel is a cutting-edge direction in the preparation of high-performance concrete.

Graphene oxide (GO) is a derivative of graphene.[4−6] The surface and edges of GO contain a large number of functional groups such as epoxy, hydroxyl, and carboxyl groups, which endow GO with new properties.[7,8] In addition, functional groups make GO have excellent hydrophilicity and high chemical compatibility and it is easy to compound with traditional materials to form new nanocomposites.[9] Jing et al. found[10] that the large specific surface area of GO served as a template for the formation of concrete hydration products, and GO filled the microdefects of concrete, thereby improving mechanical properties and durability of concrete.[10]

Valizadeh Kiamahalleh et al.[11] found that the tensile and compressive strengths of cement mortar with 0.1% GO for 28 days were increased by 53 and 91%, respectively, compared with the reference group. Lv et al.[12] discovered that the flexural and compressive strengths of cement mortar with 0.03 wt % GO for 28 days were increased by 76.2 and 86.1%, respectively, compared with the control group. A large number of studies have shown[13,14] that GO can greatly improve the mechanical strength and durability of cement-based materials and play a role in strengthening and toughening, but the strengthening efficiency varies greatly.

The difference between the strengthening−toughening effect comes from the changeable arrangement of oxygen-containing functional groups, complex stoichiometric ratio, and various spatial configurations of GO. These factors will lead to the

diversity of GO/C−S−H structural forms, interface characteristics, and interface interactions, seriously affecting the strengthening and toughening effect of GO in concrete.

The interface plays a very important role in cross-linking the bridge between GO and C−S−H and is the key to improving the mechanical properties of nanocomposites.

Gao et al.[15] introduced covalently linked glutaraldehyde molecules and water molecules into the interlayer of GO and tested their stress−strain curves. The average Young's modulus and strength of GO paper connected by glutaraldehyde molecular layers are about 30.4 GPa and 101 MPa, which are 190% and 60% higher than 10.5 GPa and 63.6 MPa of untreated GO paper, respectively. An et al.[16] found that the rigidity and strength of GO paper with 0.94% covalently bonded bromine increased by 255 and 20%, respectively. After further annealing, the Young's modulus and tensile strength can reach 127 ± 4 GPa and 185 MPa, respectively. In addition, Wan et al.[17] found that the interlayer covalent and specific noncovalent bonds were created in GO sheets, and then the mechanical properties of the composite system can be improved.

Previous studies[18−20] show that the presence of interlayer sp³ reduces the in-plane mechanical properties of double-layer graphene but improves the load transfer ability between layers.

A concept approach is to enhance the interfacial interaction between CSH and GO through interlayer covalent bonding. More importantly, can the sp³ bonds be introduced into GO to form a new configuration, which can enhance the interlayer stress transfer and even the overall performance of GO/CSH?

In this paper, a controlled improvement of interlayer stress transfer in double-layer GO/C−S−H (D-GO−CSH)-layered nanostructures is proposed by using interlayer sp³ bonds and chirality. In considering the effects of interlayer sp³ bonds, chirality, functional group types, and contents, the interlayer stress transfer and interfacial bond energies of D-GO−CSH-layered nanostructures were studied. In addition, the coupling effects of these parameters on mechanical properties of D-GO−CSH-layered nanostructures were investigated, and we tried to find the best scheme to enhance the mechanical properties of GO/CSH-layered nanostructures.

## 2. COMPUTATIONAL MODEL AND METHOD

A Large-scale Atomic/Molecular Parallel Simulator (LAMMPS) is used to achieve the simulation work.[21−23] The crystal structure of 11 Åtbermorite was assumed as the initial model. Then, all of the waters were removed from the crystal model to obtain a calcium silicon skeleton structure. Next, the silicon−oxygen tetrahedron on the silicon−oxygen (Si−O) chain in the model is deleted. Some calcium ions were added to make the final polymerization degree distribution of the Si−O tetrahedron conform to the results of nuclear magnetic resonance (NMR) test.[24] A Tobermorite 11 Å model describing the layered nanostructure of CSH is shown in Figure 1.

Next, a double-layer GO model was established, as shown in Figure 2. The functional groups of the double-layer GO model include hydroxyl (OH), epoxy (O−O), and hydroxyl + epoxy (OH + O−O) hybridization groups. The double-layer GO model with different functional groups was inserted into the center of the CSH layer, thus forming the double-layer GO/CSH interface model (D-GO−CSH) (Figure 3).
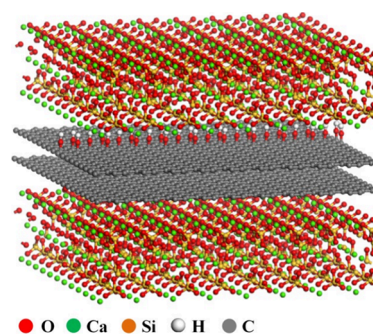
The mutual effect of layered nanostructures in the simulated works was characterized by using the Reactive Force Field
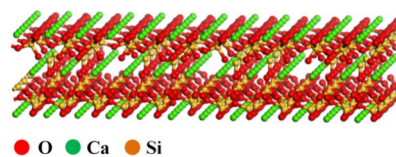
Figure 1. Schematic model of Tobermorite 11 Å (CSH-layered nanostructures). Red color, oxygen atoms; orange color, silicon atoms; green color, calcium atoms.
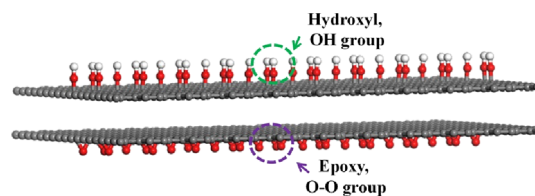
Figure 2. Double-layer GO model, including the hydroxyl (OH) and epoxy (O−O) groups.

Figure 3. Double-layer GO/CSH interface model (D-GO−CSH). Pink, boron atoms; blue, nitrogen atoms. The double-layer GO model is inserted into the center of the CSH layer.

(ReaxFF).[25−27] The interlayer sp³ bonded to the GO layer, and their interactions were described by Tersoff potential.[19,28]

By using the Verlet algorithm, the characteristics of the atomic trajectory are described. The time step is assumed to be 0.25 fs. So as to stabilize the kinetic energy, potential energy, and temperature of the simulation works, 100 ps is relaxed in the NPT ensemble. Finally, 1×10^{-3} tensile load is used to simulate all models.

3. RESULTS AND DISCUSSION

3.1. Validation. The comparison of the Young's modulus, failure strength, and strain values of CSH and GO/CSH models is obtained by the present study and by previous works, as shown in Table 1. The Young's modulus and failure strength of the CSH model in simulated works are examined respectively to be 29.6 and 1.54 GPa.

The simulated results are consistent with a previous study of Kai et al. (the Young's modulus and failure strength of CSH are 32.9 and 1.89 GPa, respectively).[30] In addition, the simulated works are also in good agreement with the previous MD results.[29,31]
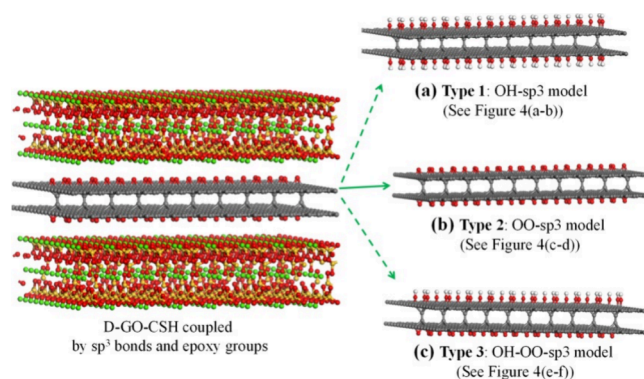
3.2. Effect of Functional Group Types Coupled by sp³ Bonds. To investigate the effects of functional group types coupled by sp³ bonds on the interlayer stress transfer of D-GO−CSH-layered nanostructures, a series of sp³ bonds were created in GO layers (See Figure 4). The control groups contain three types, D-GO−CSH with hydroxyl groups (named OH), D-GO−CSH with epoxy groups (named

Table 1. Comparing the Young's Modulus, Failure Strength, and Strain Values of CSH and GO/CSH Models Obtained by the Present Study and by Previous Works

sample	assessment method (potential)	failure strain	failure strength (GPa)	Young's modulus (GPa)	reference
CSH	MD (ReaxFF)	0.111	1.54	29.6	present study
CSH	MD (ClayFF)	0.109	1.06	27.2	Hou et al.[29]
CSH	MD (ReaxFF)	0.106	1.89	32.9	Kai et al.[30]
GO/CSH	MD (ReaxFF)	0.121	2.14	46.7	present study
GO/CSH	MD (ReaxFF)		2.33	50.2	Kai et al.[30]
GO/CSH	MD (ReaxFF)		1.50		Hou et al.[31]

Figure 5. D-GO−CSH coupled by different types of sp³ bonds. (a) Type 1: OH-sp3 model; (b) type 2: OO-sp3 model; (c) type 3: OH-OO-sp3 model.

OO), and D-GO−CSH with hydroxyl and epoxy groups (named OH-OO). When the interlayer sp³ bonds were created in three control groups, their corresponding research groups were named OH-sp3, OO-sp3, and OH-OO-sp3 models, respectively (see Figure 5).

We can see from Figure 5a,b that the D-GO−CSH interface model only contained one type of functional group. However, Figure 5c shows the GO/CSH interface model in the presence of hydroxyl and epoxy groups coupled by sp³ bonds (OH + OO-sp3). The OH + OO-sp3 model is different from the other two models, and it is more complicated. What coupling effect will the several types of functional groups have with the sp³ bond? More importantly, how will this coupling affect the interfacial interaction of D-GO−CSH-layered nanostructures?

It is difficult to visually determine the degree and difference in the interfacial interaction between the GO layer and the CSH model. Therefore, interfacial bond energies and shear stress were used to analyze the degree of interfacial interaction of the D-GO−CSH-layered nanostructures.

First, the interfacial bond energies of D-GO−CSH-layered nanostructures were supposed to be E_{total}. Then, the relationship of interfacial energies can be obtained:

$$E_{bonding} = E_{total} - (E_{C\text{-}S\text{-}H} + E_{GO} + E_{sp^3}) \quad (1)$$

where E_{sp^3} is the energies of interlayer sp³ bonds, $E_{C\text{-}S\text{-}H}$ is the energies of the CSH model, E_{GO} is the energies of GO layers, and $E_{pull\text{-}bonding}$ is the pull-out energies of D-GO−CSH-layered
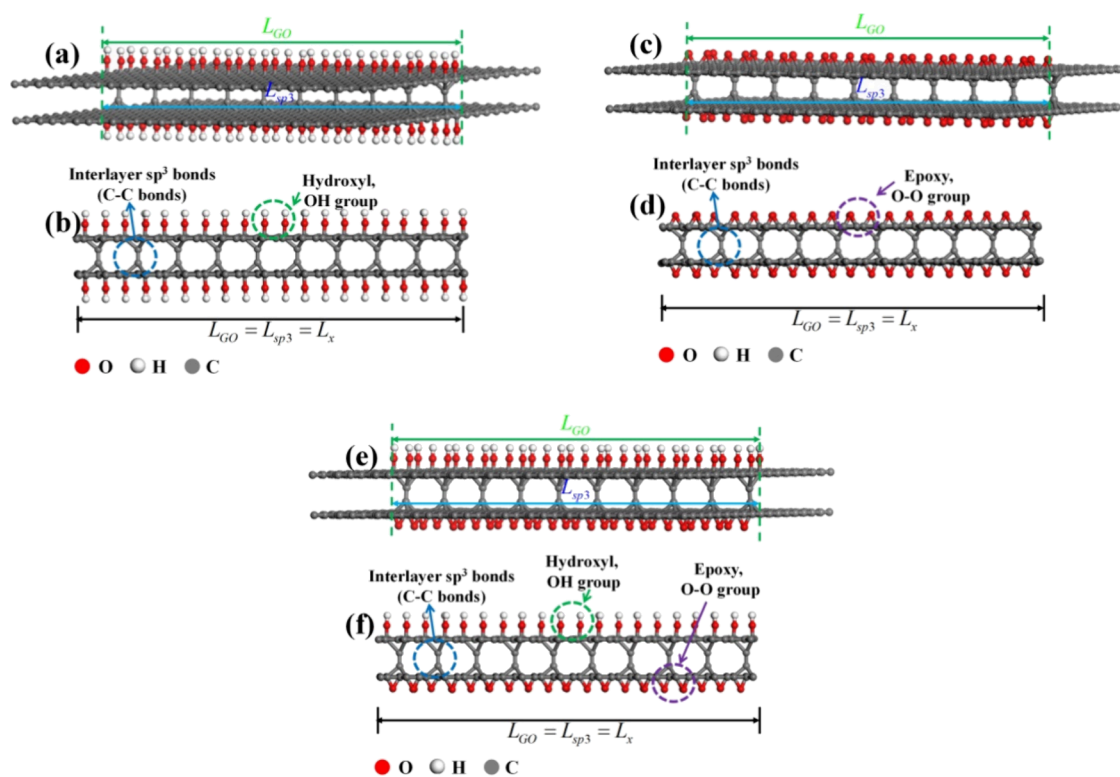
Figure 4. Schematic model of GO layers coupled by sp³ bonds. (a, b) Schematic model of hydroxyl groups coupled by sp³ bonds, (c, d) schematic model of epoxy groups coupled by sp³ bonds, and (e, f) schematic model of hydroxyl and epoxy groups coupled by sp³ bonds. L_{sp3}, L_{GO}, and L_x are lengths of interlayer sp³ bonds, functional groups, and system, respectively.

nanostructures when the GO layer is completely pulled out of the CSH model.

$$E_{\text{pull-Bonding}} = \int_{x=0}^{x=l} A\tau_i dx = \int_{x=0}^{x=l} 2S\tau_i dx = \int_{x=0}^{x=l} \chi 2$$
$$w(L-x)\tau_i dx = w\tau_i L^2 \tag{2}$$

where S is the area of the GO layer, w and L are the width and length of the GO layer, x is the coordinate of the drawing direction, χ is the proportion of interlayer sp^3 bonds in the GO layer, τ_i is the shear stress of the D-GO−CSH-layered nanostructures, and i is types of functional groups ($i = (1, 2,$ or 3)).

$$E_{\text{pull-bonding}}^{nor} = \frac{E_{\text{pull-bonding}}^{i}}{E_{\text{max}}} i = (1, 2, \text{ or } 3) \tag{3}$$

where $E_{\text{pull-bonding}}^{nor}$ is the normalized pull-out energies, and E_{max} is the maximum value of pull-out energies in all samples.

The shear stress (τ_i) in D-GO−CSH-layered nanostructures can be counted by using shear-lag theory. The D-GO−CSH-layered nanostructures were assumed to be a continuous solid substance. Then, a relationship between interfacial tensile stress ($\sigma_{\text{sp3-GO}}$), displacement, and shear stress (τ_i) can be obtained.

$$\frac{d\sigma_{\text{sp3-GO}}}{dx} = -\frac{\tau_{\text{sp3-GO}}}{t} = \gamma(u_{\text{sp3-GO}} - v_{\text{CSH}}) \tag{4}$$

where $\sigma_{\text{sp3-GO}}$ is interfacial tensile stress of a double-layer GO model, and x is the direction of tension. $\tau_{\text{sp3-GO}}$ is the interfacial shear stress of a double-layer GO model, and γ is a constant. $u_{\text{sp3-GO}}$ is the displacement of a double-layer GO model, and v_{CSH} is the displacement of a CSH model.

According to the relationship between v_{CSH} and $u_{\text{sp3-GO}}$, the interlayer stress transfer ($(Q)_{\text{test}}$) can also be calculated.

Afterward, eq 4 can be translated according to the solid mechanics theory:

$$\sigma_{\text{sp3-GO}} = E_{\text{sp3-GO}} A \varepsilon_{\text{sp3-GO}} = E_{\text{GO}} A \left(\frac{du_{\text{sp3-GO}}}{dx} \right) \tag{5}$$

where $\varepsilon_{\text{sp3-GO}}$ and $E_{\text{sp3-GO}}$ are the interfacial tensile strain and Young's modulus of a double-layer GO model, respectively. A is the cross-sectional area.

We used R_{CSH} to describe the displacement of the CSH model in the z direction.

$$\frac{dv_{\text{CSH}}}{dz} = R_{\text{CSH}} \tag{6}$$

Next, we take the second-order derivative of eq 5, then substitute eq 6 into eq 7, and finally integrate them to get eq 8.

$$\frac{d^2\sigma_{\text{sp3-GO}}}{dx^2} = \gamma \left(\frac{\sigma_{\text{sp3-GO}}}{E_{\text{p3-GO}} A} - R_{\text{CSH}} \right) \tag{7}$$

$$\sigma_{\text{sp3-GO}} = E_{\text{sp3-GO}} A R_{\text{CSH}} + \xi \sinh \theta x + \Psi \cosh \theta x \tag{8}$$

where $\theta = \sqrt{\frac{\gamma}{E_{\text{GO}} A}}$, ξ, and Ψ are constants. Considering the constraints, $\sigma_{\text{sp3-GO}} = 0$ at $L = 0$ and at $x = 0$. The equation can be derived as follows:

$$\sigma_{\text{sp3-GO}} = E_{\text{sp3-GO}} \varepsilon_{\text{sp3-GO}} \left(1 - \frac{\cosh(nx/t)}{\cosh(nL/2t)} \right) \tag{9}$$

where

$$n = \sqrt{\frac{2G_{\text{sp3-GO}}}{E_{\text{sp3-GO}}} g \frac{t}{T}} \tag{10}$$

where T is the unit cell size of D-GO−CSH-layered nanostructures in the z direction. Therefore, the interfacial shear stress of the double-layer GO model in D-GO−CSH-layered nanostructures can be obtained as follows:

$$\tau_{\text{sp3-GO}} = nE_{\text{sp3-GO}} \varepsilon_{\text{sp3-GO}} \left(\frac{\sinh(nx/L)}{\cosh(nL/2t)} \right) \tag{11}$$

By using the above equations, the normalized pull-out energies and normalized shear stress of the D-GO−CSH interface model coupled by sp^3 bonds were obtained, as shown in Figure 6. For the control groups (OH, OO, and OH-OO
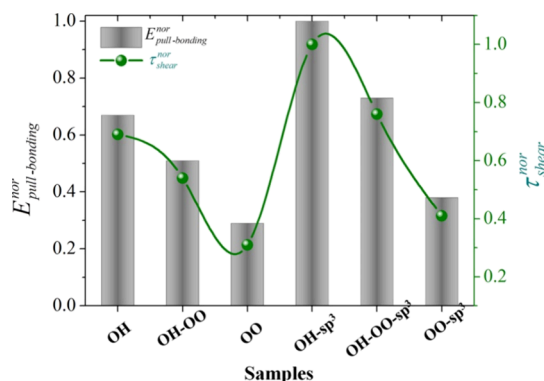
Figure 6. Normalized pull-out energies and normalized shear stress of the double-layer GO/CSH interface model coupled by sp^3 bonds. The control groups contain three types, D-GO−CSH with hydroxyl groups (named OH), D-GO−CSH with epoxy groups (named OO), and D-GO−CSH with hydroxyl and epoxy groups (named OH-OO). When the interlayer sp^3 bonds are created in three control groups, their corresponding research groups are named OH-sp3, OO-sp3, and OH-OO-sp3 models, respectively.

models), the normalized pull-out energies ($E_{\text{pull-bonding}}^{nor}$) for OH, OO, and OH-OO models are 0.29, 0.51, and 0.67, respectively. The $E_{\text{pull-bonding}}^{nor}$ between OH and CSH is greater than that between OO and CSH, which is consistent with previous research results.[32] A lower pull-out energy is due to the weak vdW interaction between the two GO layers, and their values are only about half of E_{max}. In addition, the normalized shear stress values of control groups also follow similar regularity. The normalized shear stress values ($\tau_{\text{shear}}^{nor}$) for OH, OO, and OH-OO models are 0.31, 0.54, and 0.69, respectively. This is the main reason why the GO−CSH composites in experiments cannot achieve the strength predicted in theoretical research. When GO−CSH composites are subjected to external loads, due to the weak vdW interaction between the two GO layers, the external loads cannot be transferred from the upper GO layer to the lower GO layer. Therefore, GO−CSH composites can be considered as two relatively independent configurations: One structure shows that the upper GO layer is connected to CSH, and the other structure shows that the lower GO layer is connected to CSH. The two relatively

independent configurations cannot bear the external loads together. However, this situation can be improved by adding an interlayer sp^3 bond. As shown in Figure 6, the $E_{\text{pull-bonding}}^{\text{nor}}$ and $\tau_{\text{shear}}^{\text{nor}}$ of double-layer GO/CSH interface models coupled by sp^3 bonds (OH-sp3, OO-sp3, and OH-OO-sp3 models) are greatly increased compared with the corresponding control groups. The values of $E_{\text{pull-bonding}}^{\text{nor}}$ and $\tau_{\text{shear}}^{\text{nor}}$ show a trend: OH-sp3 model>OH-OO-sp3 model>OO-sp3 model. Clearly, the presence of interlayer sp^3 bonds in double GO layers can enhance the interfacial interaction and overall coherence of double GO layers and the CSH matrix. In addition, the degree of enhancement is closely related to the coupling effects between interlayer sp^3 bonds and the functional group types. On the OH-sp3 model, $E_{\text{pull-bonding}}^{\text{nor}}$ has the highest degree of enhancement, with an increase of 49.25% compared to the OH model. However, the enhancement degree of $E_{\text{pull-bonding}}^{\text{nor}}$ in the OO-sp3 model is relatively low, which is 31.03% higher than that in the OO model. Although the enhancement effect of interlayer sp^3 bonds on the strong bonding interface (OH and CSH) is greater than that of the weak bonding interface (OO and CSH), it can still increase $E_{\text{pull-bonding}}^{\text{nor}}$ and $\tau_{\text{shear}}^{\text{nor}}$ by 31.03 and 32.25%, respectively. These findings provide a new idea for strengthening the mechanical properties of layered nanostructure materials.

The maximum value of interlayer stress transfer was assumed to be 1. The results were compared by using normalized interlayer stress transfer (eq 12).

$$Q_{\text{nor}} = \frac{(Q)_{\text{test}}}{(Q)_{\text{max}}} \tag{12}$$

where Q_{nor} is the normalized interlayer stress transfer, $(Q)_{\text{test}}$ is the interlayer stress transfer of the simulated model, and $(Q)_{\text{max}}$ is the maximum values of interlayer stress transfer in the simulated model.

It can be seen from Figure 7 that the normalized interlayer stress transfer (Q_{nor}) of the simulated models increases with
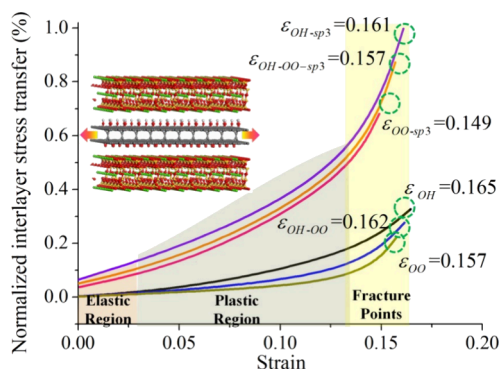
Figure 7. Interlayer stress transfer of the double-layer GO/CSH interface model coupled by sp^3 bonds with a change of strain.

the increase in strain. The Q_{nor} of all simulated models can be divided into three stages: elastic stage, plastic stage, and failure stage. In the elastic stage, the Q_{nor} value of the simulation model increases slowly, indicating that the deformation is still elastic. The values of Q_{nor} are relatively small and remain at 0 to 0.2. The interlayer sp^3 bonds have not been subjected to distorted stress from the GO and C−S−H layers. In the plastic stage, their normalized interlayer stress transfer grows rapidly from 0.2 to about 0.5, implying that irreversible plastic

deformation is caused. Finally, the maximum values of Q_{nor} in simulated models stay at the failure strain. For example, the maximum value of Q_{nor} in the OH-OO-sp3 model is 0.872 when the failure strain is 0.157. Also, the maximum value of Q_{nor} in the OH-OO model is 0.278 when the failure strain is 0.161. The failure strain of the OH-OO-sp3 model is 0.004 lower than that of the OH-OO model, but the Q_{nor} value of the OH-OO-sp3 model is 3.14 times that of the OH-OO model. Although the initial strain induced by sp^3 bonds has a negative effect on the failure stress of the D-GO−CSH model, the load transfer of the D-GO−CSH model increases exponentially. In addition, the Q_{nor} values are closely related to the coupling effect between interlayer sp^3 bonds and functional group types. This result is also consistent with the previous values of $E_{\text{pull-bonding}}^{\text{nor}}$ and $\tau_{\text{shear}}^{\text{nor}}$.

3.3. Coupling Effect of sp^3 Bond Fractions and Functional Group Contents.
Next, we turn our attention to the coupling effect of sp^3 bond fractions and functional group contents on the interfacial interaction of the double-layer GO/CSH interface model coupled by sp^3 bonds. L_{GO} is the length of the double-layer GO model, L_{sp3} is the length of interlayer sp^3 bonds on the double-layer GO model, and L_x is the length of the simulated system.
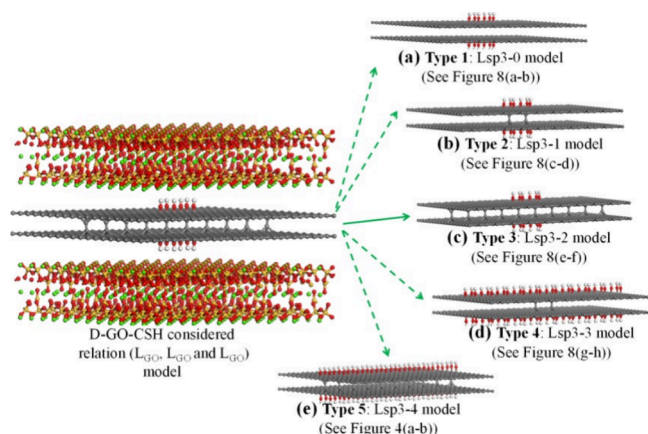
The double-layer GO/CSH interface model (containing an OH group without interlayer sp^3 bonds) was assumed to be the control group. The control group containing $L_{\text{GO}} = \frac{1}{6}L_x$ was named Lsp3-0 (see Figure 8a,b). When $L_{\text{GO}} = L_{\text{sp3}} = \frac{1}{6}L_x$, the simulated model is named Lsp3-1 (see Figure 8c,d). When $L_{\text{GO}} = \frac{1}{6}L_{\text{sp3}} = \frac{1}{6}L_x$, the simulated model is named Lsp3-2 (see Figure 8e,f). When $\frac{1}{6}L_{\text{GO}} = L_{\text{sp3}} = \frac{1}{6}L_x$, the layered model is named Lsp3-3 (see Figure 8g,h). Next, when $L_{\text{GO}} = L_{\text{sp3}} = L_x$, the simulated model is called Lsp3-4, which is similar to that in Figure 4a.

Finally, the double-layer GO/CSH interfaces coupled by these relation models are shown in Figure 9.

The normalized pull-out energies and normalized shear stress of relationship models between L_{GO}, L_{sp3}, and L_x are shown in Figure 10. It is shown that $E_{\text{pull-bonding}}^{\text{nor}}$ and $\tau_{\text{shear}}^{\text{nor}}$ increase from 0.11 and 0.17 for the control group to 0.31 and 0.36 for the Lsp3−2 model, respectively. The $E_{\text{pull-bonding}}^{\text{nor}}$ and $\tau_{\text{shear}}^{\text{nor}}$ values of the Lsp3-1 model are almost 2 times higher than its control group. Clearly, the $E_{\text{pull-bonding}}^{\text{nor}}$ and $\tau_{\text{shear}}^{\text{nor}}$ of simulated models increase with an increase in L_{GO} and L_{sp3}. When the interlayer sp^3 bonds do not exist, the $E_{\text{pull-bonding}}^{\text{nor}}$ and $\tau_{\text{shear}}^{\text{nor}}$ of the simulated model are mainly dominated by weak van der Waals forces. When the interlayer sp^3 bonds exist ($L_{\text{sp3}} = \frac{1}{6}L_x$), in addition to the van der Waals interaction, the D-GO−CSH interface model also increases interlayer covalent interaction. With only a low fraction of interlayer sp^3 bonds in the D-GO−CSH interface model, the $E_{\text{pull-bonding}}^{\text{nor}}$ and $\tau_{\text{shear}}^{\text{nor}}$ values of Lsp3-1 model are 0.14 and 0.21, which are 27.27 and 23.53% higher than that of the control group. It is worth noting that the $E_{\text{pull-bonding}}^{\text{nor}}$ and $\tau_{\text{shear}}^{\text{nor}}$ of the Lsp3-3 model grew rapidly and reached the maximum of 0.84 and 0.86 when $\frac{1}{6}L_{\text{GO}} = L_{\text{sp3}} = \frac{1}{6}L_x$. This is because the mechanical strength of the GO−CSH interface comes from hydrogen bonding.[29] The more the OH groups of the D-GO−CSH interface model reacted with silicate chains in the CSH matrix, the more hydrogen bonding created and the greater the improvement of interfacial interaction of GO and the CSH matrix will be.
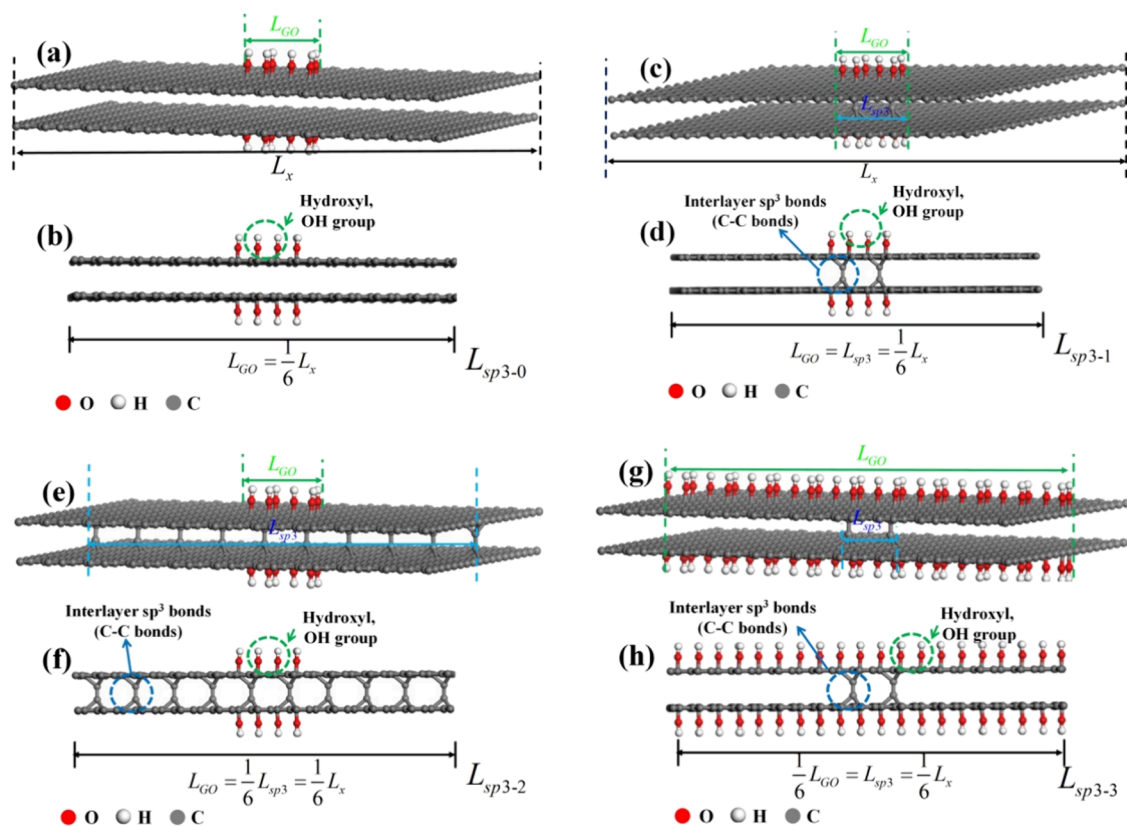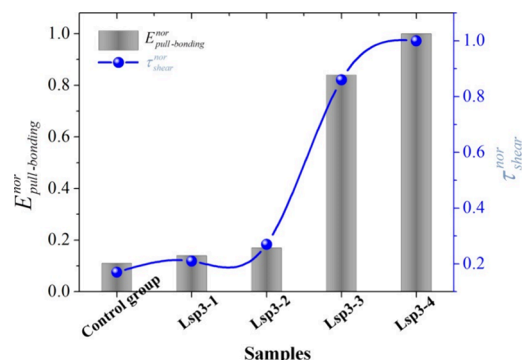
Figure 8. Relationship models between L_{GO}, L_{sp3}, and L_x. (a, b) Relationship model of the control group, $L_{GO} = \frac{1}{6}L_x$ (Lsp3-0), (c, d) relationship model of $L_{GO} = L_{sp3} = \frac{1}{6}L_x$ (Lsp3-1), (e-f) relationship model of $L_{GO} = \frac{1}{6}L_{sp3} = \frac{1}{6}L_x$ (Lsp3-2), and (g, h) relationship model of $\frac{1}{6}L_{GO} = L_{sp3} = \frac{1}{6}L_x$ (Lsp3-3).

Figure 9. Double-layer GO/CSH interfaces coupled by relationship models between L_{GO}, L_{sp3}, and L_x. (a) Type 1: Lsp3-0 model; (b) type 2: Lsp3-1 model; (c) type 3: Lsp3-2 model; (d) type 4: Lsp3-3 model; (e) type 5: Lsp3-4 model.

Figure 10. Normalized pull-out energies and normalized shear stress of double-layer GO/CSH interfaces coupled by relationship models between L_{GO}, L_{sp3}, and L_x.

Furthermore, a higher improvement of $E_{pull-bonding}^{nor}$ and τ_{shear}^{nor} at the Lsp3-4 model, relative to the Lsp3-3 model, can be attributed to the fact that interlayer sp^3 bonds can help functional groups to better interact with the CSH matrix.
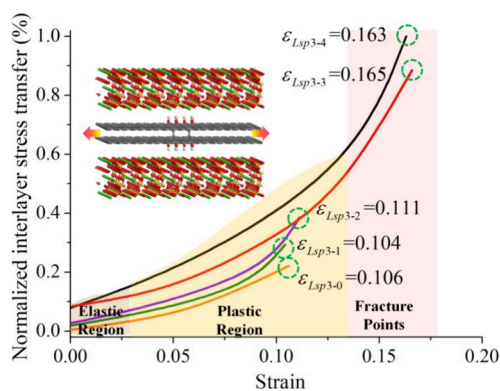
Interlayer stress transfer of relationship models between L_{GO}, L_{sp3}, and L_x with a change of strain iss shown in Figure 11. It is found that the value of Q_{nor} grows the fastest with the increase in strain, and its result is consistent with that of $E_{pull-bonding}^{nor}$ and τ_{shear}^{nor}. In addition, the Q_{nor} value increases from 0.221 for the control group ($L_{GO} = \frac{1}{6}L_x$, Lsp3-0) to 0.293 for the Lsp3-1 model ($L_{GO} = L_{sp3} = \frac{1}{6}L_x$). The Q_{nor} value of the Lsp3-1 model is 32.58% higher than that of its control group. Nevertheless, the failure strain of the Lsp3-1 model has only a little reduction (almost 2%) compared with the Lsp3-0 model. Although interlayer sp^3 bonds increased the initial strain of GO and reduced the in-plane stress of GO, resulting in a little decrease in strain of the system, clearly, the Q_{nor} value is significantly increased when adding the sp^3 bonds and functional groups.

**3.4. Coupling Effect of Interlayer sp^3 Bonds and Chirality.** D-GO−CSH models coupled by interlayer sp^3

Figure 11. Interlayer stress transfer of double-layer GO/CSH interfaces coupled by relationship models between L_{GO}, L_{sp3}, and L_x with a change of strain.

bonds and chirality were established (see Figure 12): a OH group at the edge and at the center region. For each region,
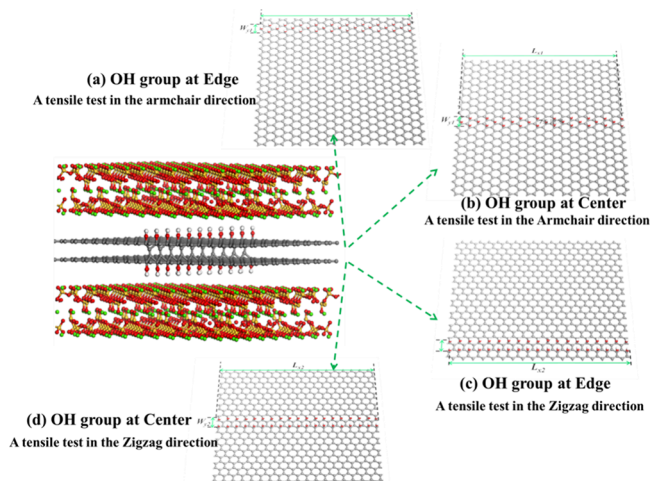
Figure 12. Double-layer GO/CSH interfaces coupled by sp³ bonds and chirality when $L_{sp3} = L_{GO} = L_x$. (a) OH group at the edge region in the GO layer when tensile stress is applied in the armchair direction (armchair-edge), (b) OH group at the center region in the GO layer when tensile stress is applied in the armchair direction (armchair-cen), (c) OH group at the edge region in the GO layer when tensile stress is applied in the zigzag direction (zigzag-edge), and (d) OH group at the center region in the GO layer when tensile stress is applied in the zigzag direction (zigzag-cen). The L_{x1} and W_{y1} are the length and width of sp³ bonds on (a) and (b) models. The L_{x2} and W_{y2} are the length and width of sp³ bonds on (c) and (d) models.

different cases of chirality have been investigated, including different chirality of GO (armchair and zigzag) and different locations of GO (edge and at the center region). The normalized pull-out energies and normalized shear stress of D-GO−CSH models coupled by interlayer sp³ bonds and chirality are shown in Figure 13. It is found that the $E_{pull-bonding}^{nor}$ and τ_{shear}^{nor} values are closely related to chirality and sp³ bond positions of D-GO−CSH models. When tensile stress is applied in the armchair direction, the $E_{pull-bonding}^{nor}$ and τ_{shear}^{nor} values of the armchair-edge model were found to be 0.64 and 0.69, respectively, which are lower than those of the armchair-cen model. This larger improvement of the $E_{pull-bonding}^{nor}$ and τ_{shear}^{nor} values at the armchair-cen model, relative to the armchair-edge model, can be attributed to the fact that the interlayer sp³
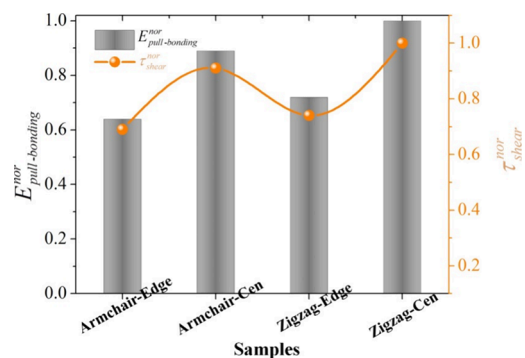
Figure 13. Normalized pull-out energies and normalized shear stress of D-GO−CSH models coupled by interlayer sp³ bonds and chirality, including the armchair-edge, armchair-cen, zigzag-edge, and zigzag-cen models.

bonds in the center of the GO layer can transfer the distorted stress to two sides, while the interlayer sp³ bonds at the edge of GO only transfer the distorted stress to one side.

Compared with the armchair-edge model, the sp³ bonds in the edge of the GO layer (zigzag-edge) result in 12.5 and 7.2% improvement in $E_{pull-bonding}^{nor}$ and τ_{shear}^{nor}. Also, the $E_{pull-bonding}^{nor}$ and τ_{shear}^{nor} of the zigzag-cen model are 12.36 and 9.89% higher than those of armchair-cen model, respectively. It is attributable to a greater torsion of the bond angle in the zigzag direction to adapt the external load. Compared with armchair's model, the zigzag model can withstand a higher deformation of bond length and bond angle. The detailed deformation model of bond length and bond angle is shown in Figure 14.
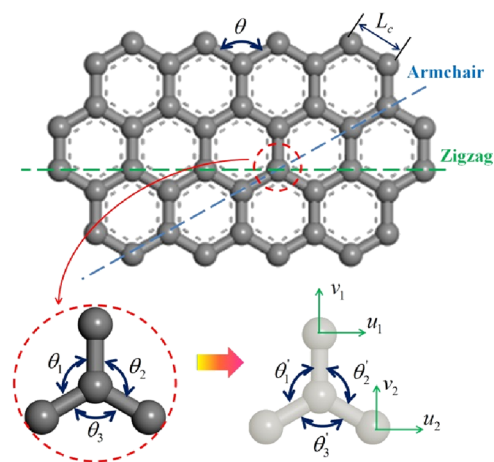
Figure 14. Detailed deformation model of bond length and bond angle.

To further investigate the change of bond length, bond angle, and bond strain energy in armchair and zigzag models, the strain energy percentage of D-GO−CSH models with different chirality was studied.

The Δr is supposed to be the change of bond length, $\Delta \Phi$ is supposed to be the change of bond angle, and $\Delta \varpi$ is the change of torsion angle.

According to the fracture mechanics theory, the strain energy (U_{GO}) about bond lengths and bond angles at the GO layer can be defined by eqs 13 and 14.

$$U_{\text{Bond-GO}} = q \sum_{e=1}^{3} \int_{r_{\text{GO}_0}}^{r_{\text{GO}_i}} \frac{1}{2} F_{\text{GO}} \sin \theta_{\text{GO}} dr_{\text{GO}} \tag{13}$$

$$U_{\text{Angle-GO}} = q \sum_{e=1}^{3} \int_{\theta_{\text{GO}_0}}^{\theta_{\text{GO}_i}} M_{\text{GO}} \theta_{\text{GO}} d\theta_{\text{GO}} \tag{14}$$

where $U_{\text{Bond-GO}}$ is the strain energy related to bond lengths at the GO layer, and $U_{\text{Angle-GO}}$ is the strain energy related bond angles at the GO layer. r_{GO_0} and θ_{GO_0} are bond lengths and angles, respectively, at the GO layer during the initial equilibrium state. r_{GO_i} and θ_{GO_i} are bond lengths and angles, respectively, at the GO layer after the tension state. F_{GO} is the force on the GO layer, and M is the bending moment. e is the coefficient.

Finally, the total strain energy percentage can be calculated by the following equation (eq 15).

$$S_{\text{GO}} = \frac{U_{\text{Bond-GO}}}{U_{\text{Bond-GO}} + U_{\text{Angle-GO}}} \tag{15}$$

where S_{GO} is the change of bond length and bond angle of the GO layer with strain energy.

Figure 15 shows the strain energy percentage of D-GO–CSH models coupled by interlayer sp^3 bonds and chirality,
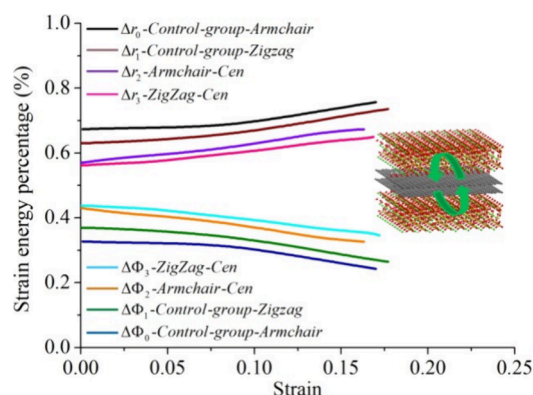
Figure 15. Strain energy percentage of D-GO–CSH models coupled by interlayer sp^3 bonds and chirality. Δr is the proportion of strain energy to the change in bond lengths, and $\Delta\Phi$ is the proportion of strain energy to the change in bond angles.

including control groups (without sp^3 bonds, named control-group-armchair and control-group-zigzag), the zigzag-cen model, and the armchair-cen model. The results show that the bond length changes (Δr) of D-GO–CSH models coupled by interlayer sp^3 bonds and chirality increase with an increase in strain, while their bond angle changes ($\Delta\Phi$) decrease with an increase in strain. Among them, an obvious trend was shown: $\Delta r_0 > \Delta r_1 > \Delta r_2 > \Delta r_3$ and $\Delta\Phi_0 < \Delta\Phi_1 < \Delta\Phi_2 < \Delta\Phi_3$.

For the control-group-armchair model, the difference between Δr_0 and $\Delta\Phi_0$ is the largest, which is 0.515. In this case, the influence of Δr_0 is not obvious compared with $\Delta\Phi_0$. The change of Δr_0 is the main factor affecting mechanical properties; however, the influence of $\Delta\Phi_0$ is relatively weak, and the system breaks directly after Δr_0 reaches the cutting radius. Similar to the control-group-armchair model, the control-group-zigzag model also has a relatively larger difference (0.471) between Δr_1 and $\Delta\Phi_1$. However, the difference between Δr_1 and $\Delta\Phi_1$ of the control-group-zigzag

model gradually narrows with the increase in strain. It is found that the difference between the Δr and $\Delta\Phi$ of the zigzag model is smaller than those of the armchair model, indicating that $\Delta\Phi$ plays a role in guiding stress deflection.

Next, we pay attention to the effect of sp^3 bonds on Δr and $\Delta\Phi$. The difference between Δr_2 and $\Delta\Phi_2$ in the armchair-cen model is 0.348. Under the external load, the changes of Δr_2 and $\Delta\Phi_2$ of the armchair-cen model are significant and both changes cannot be ignored. In addition, we also found that the difference between Δr_3 and $\Delta\Phi_3$ in the zigzag-cen model is only 0.307, implying that Δr_3 did not reach the cutoff distance, but the change in $\Delta\Phi_3$ was very significant. In this case, the structural failure is due to the change of $\Delta\Phi_3$, and the in-plane distortion stress is effectively deflected and bifurcated.

The difference between Δr_3 and $\Delta\Phi_3$ in the zigzag-cen model is 34.8% lower than Δr_1 and $\Delta\Phi_1$ in the control group zigzag model. The interlayer sp^3 bonds have a remarkably positive influence on the change of $\Delta\Phi$.

Figure 16 shows the normalized interlayer stress transfer (Q_{nor}) of D-GO–CSH models coupled by interlayer sp^3 bonds
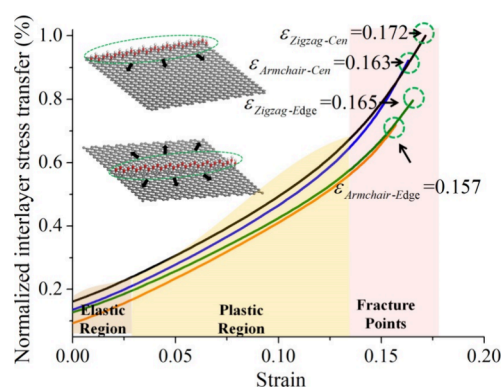
Figure 16. Normalized interlayer stress transfer of D-GO–CSH models coupled by interlayer sp^3 bonds and chirality with a change of strain.

and chirality with a change of strain, including the armchair-edge, armchair-cen, zigzag-edge, and zigzag-cen models.

As can be seen from Figure 16, the Q_{nor} value of the four models is increased with the increase in strain. In the elastic stage, their Q_{nor} value increases slowly, while in the plastic stage, their Q_{nor} value increases rapidly. Finally, the Q_{nor} values of armchair-edge, armchair-cen, zigzag-edge, and zigzag-cen models remained at their maximum strain they can withstand, which are 0.172, 0.163, 0.165, and 0.157, respectively. It shows a trend in the Q_{nor} value: zigzag-cen > armchair-cen > zigzag-edge > armchair-edge. In the same sp^3 bond location, the Q_{nor} value of the zigzag-cen model is greater than that of armchair-cen model. The results are also consistent with the values of Δr and $\Delta\Phi$.

In the armchair model, the Q_{nor} value of the armchair-cen model is greater than that of the armchair-edge model. This is mainly because the sp^3 bonds are located at the edge of the GO layer, and the stress area it can transfer is limited. However, the sp^3 bonds are located at the center of the GO layer, and the stress area it can transfer is greatly enhanced.

4. CONCLUSIONS

In this paper, it is proposed to control and improve the interlayer stress transfer in double-layer GO/C–S–H-layered

nanostructures by using the interlayer sp^3 bonds and chirality on the GO layer. Considering the influence of sp^3 bond location, sp^3 bond fraction, chirality, and type and content of functional groups, the interlayer stress transfer and interface bond energies of double-layer GO/C−S−H-layered nanostructures were studied.

In considering the coupling effect of functional group types and sp^3 bonds, the values of $E_{\text{pull-bonding}}^{\text{nor}}$ and $\tau_{\text{shear}}^{\text{nor}}$ show a trend: OH-sp3 model > OH-OO-sp3 model > OO-sp3 model. Compared with the control group, the normalized shear stress and normalized pull-out energy of the OH-sp3 model are increased by 44.93 and 49.25%, respectively, while those of the OO-sp3 model are increased by 32.26 and 31.03%, respectively.

In considering the coupling effect of sp^3 bond fractions and functional group contents, the $E_{\text{pull-bonding}}^{\text{nor}}$ and $\tau_{\text{shear}}^{\text{nor}}$ of simulated models increase with an increase in L_{GO} and L_{sp3}. In addition, the Q_{nor} value of the Lsp3-1 model is 32.58% higher than that of its control group. Nevertheless, the failure strain of the Lsp3-1 model has only a little reduction (almost 2%) compared with the Lsp3-0 model.

In considering the coupling effect of interlayer sp^3 bonds and chirality, the $E_{\text{pull-bonding}}^{\text{nor}}$ and $\tau_{\text{shear}}^{\text{nor}}$ values are closely related to chirality and sp^3 bond position of D-GO−CSH models. Compared with the armchair-edge model, the sp^3 bonds in the edge of the GO layer (zigzag-edge) result in 12.5 and 7.2% improvement in $E_{\text{pull-bonding}}^{\text{nor}}$ and $\tau_{\text{shear}}^{\text{nor}}$, respectively. Also, the $E_{\text{pull-bonding}}^{\text{nor}}$ and $\tau_{\text{shear}}^{\text{nof}}$ of the zigzag-cen model are 12.36 and 9.89% higher than those of the armchair-cen model.

Furthermore, the bond length changes (Δr) of D-GO−CSH models coupled by interlayer sp^3 bonds and chirality increase with an increase in strain, while their bond angle changes ($\Delta \Phi$) decrease with an increase in strain. The strain energy percentage difference (bond length and bond angle) of the zigzag-cen model is 34.8% lower than that of the control group model based on the fracture mechanic theory and molecular dynamics results.

Clearly, the interlayer sp^3 bonds lead to a great enhancement (more than 3 times) in normalized interlayer stress transfer of D-GO−CSH-layered nanostructures while exerting a little opposite effect (about 5%). It is confirmed that the interlayer sp^3 bonds have a remarkably positive effect on the interlayer stress transfer of the D-GO−CSH-layered nanostructures.

It provides a new approach to actively control the interlayer stress transfer, pull-out energy, and interlayer shear stress of D-GO−CSH-layered nanostructures.

■ AUTHOR INFORMATION

Corresponding Author

Lei Fan − *School of Civil Engineering and Architecture, Zhejiang University of Science & Technology, Hangzhou 310023, PR China;* ⊙ orcid.org/0000-0002-8018-4174; Email: fanleigl@foxmail.com

Authors

Fangyuan Song − *School of Civil Engineering and Architecture, Zhejiang University of Science & Technology, Hangzhou 310023, PR China*

Jingjing Xu − *Henan Finance University, Zhengzhou, Henan 450000, PR China*

Hongwei Wang − *School of Civil Engineering and Architecture, Zhejiang University of Science & Technology, Hangzhou 310023, PR China*

Fengzhi Wang − *School of Civil Engineering and Architecture, Zhejiang University of Science & Technology, Hangzhou 310023, PR China*

Complete contact information is available at:
https://pubs.acs.org/10.1021/acsomega.3c07943

■ REFERENCES

(1) Zhou, F.; Pan, G.; Mi, R.; Zhan, M. Improving the properties of concrete using in situ grown C-S-H. *Constr. Build. Mater.* **2021**, *276*, No. 122214.

(2) Wang, J. W.; Gao, C.; Tang, J. H.; Hu, Z. L.; Liu, J. P. The multi-scale mechanical properties of calcium-silicate-hydrate. *Cement and Concrete Composites* **2023**, *140*, No. 105097.

(3) Hu, C.; Ruan, Y.; Yao, S.; Wang, F.; He, Y.; Gao, Y. Insight into the evolution of the elastic properties of calcium-silicate-hydrate (C-S-H) gel. *Cem. Concr. Compos.* **2019**, *104*, No. 103342.

(4) Tamang, S.; Rai, S.; Bhujel, R.; Bhattacharyya, N. K.; Swain, B. P.; Biswas, J. A concise review on GO, rGO and metal oxide/rGO composites: Fabrication and their supercapacitor and catalytic applications. *J. Alloys Compd.* **2023**, *947*, No. 169588.

(5) Khabibrakhmanov, A. I.; Sorokin, P. B. Electronic properties of graphene oxide: nanoroads towards novel applications. *Nanoscale* **2022**, *14*, 4131−4144.

(6) Le, H. N.; Thai, D.; Nguyen, T. T.; Dao, T. B. T.; Nguyen, T. D.; Tieu, D. T.; Ha Thuc, C. N. Improving safety and efficiency in graphene oxide production technology. *J. Mater. Res. Technol.* **2023**, *24*, 4440−4453.

(7) Xu, C.; Yuan, R. S.; Wang, X. Selective reduction of graphene oxide. *New Carbon Materials* **2014**, *29*, 61−66.

(8) Shams, M.; Guiney, L. M.; Huang, L. J.; Ramesh, M.; Yang, X. N.; Hersam, M. C.; Chowdhury, I. Influence of functional groups on the degradation of graphene oxide nanomaterials. *Environmental Science-Nano* **2019**, *6*, 2203−2214.

(9) Bu, Y. S.; Li, K. J.; Guo, F.; Liang, Z.; Zhang, J. L. Mechanical behavior and failure mechanism of multilayer graphene oxides with various oxygen contents and functional types: A ReaxFF molecular dynamics simulation. *Appl. Surf. Sci.* **2022**, *606*, No. 154920.

(10) Jing, G. J.; Wu, J. J. M.; Lei, T. Y.; Wang, S. X.; Strokova, V.; Nelyubova, V.; Wang, M. J.; Ye, Z. M. From graphene oxide to reduced graphene oxide: Enhanced hydration and compressive strength of cement composites. *Construction and Building Materials* **2020**, *248*, No. 118699.

(11) Valizadeh Kiamahalleh, M.; Gholampour, A.; Tran, D. N. H.; Ozbakkaloglu, T.; Losic, D. Physiochemical and mechanical properties of reduced graphene oxide-cement mortar composites: Effect of reduced graphene oxide particle size[J]. *Constr. Build. Mater.* **2020**, *250*, No. 118832.

(12) Lv, S.H.; Zhang, J.; Luo, X.Q.; Zhu, L.L.; Ni, C.H. Microstructure and properties for composites of graphene oxide/cement. *Chin. J. Mater. Res.* **2018**, *32* (3), 233−240.

(13) Tragazikis, I. K.; Dassios, K. G.; Dalla, P. T.; Exarchos, D. A.; Matikas, T. E. Acoustic emission investigation of the effect of graphene on the fracture behavior of cement mortars[J]. *Engineering Fracture Mechanics* **2019**, *210*, 444−451.

(14) Du, S.; Jiang, Y.; Zhong, J.; Ge, Y.; Shi, X. Surface abrasion resistance of high-volume fly ash concrete modified by graphene

oxide: Macro-and micro-perspectives[J]. *Constr. Build. Mater.* **2020**, *237*, 117686−16.

(15) Gao, Y.; Liu, L.Q.; Zu, S.Z.; Peng, K.; Zhou, D.; Han, B.H.; Zhang, Z. The effect of inter layer adhesion on the mechanical behaviors of macroscopic graphene oxide papers. *ACS Nano* **2011**, *5*, 2134−2141.

(16) An, Z.; Compton, O. C.; Putz, K. W.; Brinson, L. C.; Nguyen, S. T. Bio-inspired borate cross-linking in ultra-stiff graphene oxide thin films. *Adv. Mater.* **2011**, *23*, 3842.

(17) Wan, S. J.; Li, Y. C.; Mu, J. K.; Aliev, A. E.; Fang, S. L.; Kotov, N. A.; Jiang, L.; Cheng, Q. F.; Baughman, R. H. Sequentially bridged graphene sheets with high strength, toughness, and electrical conductivity. *Proc. Natl. Acad. Sci. U.S.A.* **2018**, *115*, 5359−5364.

(18) Fan, L.; Cai, X. Y.; Wang, H. W.; Ye, J.; Feng, Y.; Huang, Z. Y.; Qu, C. Topological defects and nanoholes in graphene oxide/hexagonal boron nitride heterostructures: stress buildup and accumulation. *RSC Adv.* **2022**, *12*, 33988−34005.

(19) Fan, L.; Bian, Z. G.; Huang, Z. Y.; Song, F. Y.; Xia, Y. Q.; Xu, J. New insight into bonding energy and stress distribution of graphene oxide/hexagonal boron nitride: Functional group and grain boundary effect. *Diamond Relat. Mater.* **2022**, *127*, No. 109185.

(20) Zhang, Y. Y.; Wang, C. M.; Cheng, Y.; Xiang, Y. Mechanical properties of bilayer graphene sheets coupled by sp3 bonding. *Carbon* **2011**, *49*, 4511−4517.

(21) Fan, L.; Cai, X. Y.; Wang, H. W.; Ye, J.; Hong, Y. H.; Ying, J. H. Toughening two-dimensional hybrid materials by integrating carbon nanotubes. *Surfaces and Interfaces* **2023**, *36*, No. 102559.

(22) Fan, L.; Bian, Z. G.; Huang, Z. Y.; Song, F. Y.; Xia, Y. Q.; Xu, J. Role of grain boundary and nanoholes in geometrical deformation and bonding energies of graphene/hexagonal boron nitride. *Diamond Relat. Mater.* **2022**, *126*, No. 109119.

(23) Fan, L.; Liu, K.; Liu, G. Y.; Hong, Y. H. Defects in Gr/h-BN nanoribbons heterostructure: atomically precise cutting and defect amplification effect via hydrogenation pseudo-crack. *Diamond Relat. Mater.* **2022**, *123*, No. 108877.

(24) Zhou, Y.; Orozco, C. A.; Duque-Redondo, E.; Manzano, H.; Geng, C. Q.; Feng, P.; Monteiro, P. J. M.; Miao, C. W. Modification of poly(ethylene glycol) on the microstructure and mechanical properties of calcium silicate hydrates. *Cement and Concrete Composites* **2019**, *115*, 20−30.

(25) Liang, Y. Z. Nanoscale insight into structural characteristics and dynamic properties of C-S-H after decalcification by reactive molecular dynamics simulations. *Materials Today Communications* **2022**, *33*, No. 104684.

(26) Yang, J.; Zhang, W.; Hou, D. S.; Zhang, G. Z.; Ding, Q. J. Structure, dynamics and mechanical properties evolution of calcium silicate hydrate induced by dehydration and dihydroxylation. *Construction and Building Materials* **2021**, *291*, No. 123327.

(27) Kai, G.; Miaohong, H.; Wenhao, P.; Jinguo, W. Molecular dynamics of C-S-H production in graphene oxide environment. *Rev. Adv. Mater. Sci.* **2022**, *61*, 90−101.

(28) Yao, W. J.; Fan, L. Defects in graphene/h-BN planar heterostructures: Insights into the interfacial thermal transport properties. *Nanomaterials* **2021**, *11* (2), 500.

(29) Hou, D. S.; Zhu, Y.; Lu, Y. Y.; Li, Z. J. Mechanical properties of calcium silicate hydrate (C-S-H) at nano-scale: A molecular dynamics study. *Mater. Chem. Phys.* **2014**, *146*, 503−511.

(30) Kai, M. F.; Zhang, L. W.; Liew, K. M. Graphene and graphene oxide in calcium silicate hydrates: Chemical reactions, mechanical behaviors and interfacial sliding. *Carbon* **2019**, *146*, 181−193.

(31) Hou, D. S.; Lu, Z. Y.; Li, X. Y.; Ma, H. Y.; Li, Z. J. Reactive molecular dynamics and experimental study of graphene-cement composites: Structure, dynamics and reinforcement mechanisms. *Carbon* **2017**, *115*, 188−208.

(32) Hou, D. S.; Yang, T. J.; Tang, J. H.; Li, S. C. Reactive force field Molecular dynamics study on graphene oxide reinforced cement composite: functional groups de-protonation, interfacial bonding and strengthening mechanism. *Phys. Chem. Chem. Phys.* **2018**, *20* (13), 8773−8789.